














Publication Year	2020
Acceptance in OA	2021-12-27T11:56:24Z
Title	FAUST I. The hot corino at the heart of the prototypical Class I protostar L1551 IRS5
Authors	Bianchi, E., Chandler, C. J., Ceccarelli, C., CODELLA, CLAUDIO, Sakai, N., López-Sepulcre, A., Maud, L. T., Moellenbrock, G., Svoboda, B., Watanabe, Y., Sakai, T., Ménard, F., Aikawa, Y., Alves, F., Balucani, N., Bouvier, M., Caselli, P., Caux, E., Charnley, S., Choudhury, S., De Simone, M., Dulieu, F., Durán, A., Evans, L., Favre, C., FEDELE, DAVIDE, Feng, S., FONTANI, FRANCESCO, Francis, L., Hama, T., Hanawa, T., Herbst, E., Hirota, T., Imai, M., Isella, A., Jiménez-Serra, I., Johnstone, D., Kahane, C., Lefloch, B., Loinard, L., Maureira, M. J., MERCIMEK, SEYMA, Miotello, A., Mori, S., Nakatani, R., Nomura, H., Oba, Y., Ohashi, S., Okoda, Y., Ospina-Zamudio, J., Oya, Y., Pineda, J., PODIO, LINDA, Rimola, A., Cox, D. Segura, Shirley, Y., TAQUET, VIANNEY DANIEL FRANCOIS, TESTI, Leonardo, Vastel, C., Viti, S., Watanabe, N., Witzel, A., Xue, C., Zhang, Y., Zhao, B., Yamamoto, S.
Publisher's version (DOI)	10.1093/mnrasl/slaa130
Handle	http://hdl.handle.net/20.500.12386/31252
Journal	MONTHLY NOTICES OF THE ROYAL ASTRONOMICAL SOCIETY. LETTERS
Volume	498

FAUST I. The hot corino at the heart of the prototypical Class I protostar L1551 IRS5

E. Bianchi ¹★, C. J. Chandler,² C. Ceccarelli ¹★, C. Codella,^{1,3}★ N. Sakai ⁴, A. López-Sepulcre,^{1,5} L. T. Maud,⁶ G. Moellenbrock,² B. Svoboda,² Y. Watanabe ⁷, T. Sakai,⁸ F. Ménard,¹ Y. Aikawa,⁹ F. Alves,¹⁰ N. Balucani ¹¹, M. Bouvier,¹ P. Caselli,¹² E. Caux,¹³ S. Charnley,¹⁴ S. Choudhury,¹⁰ M. De Simone,¹ F. Dulieu,¹⁵ A. Durán,¹⁶ L. Evans,^{3,13} C. Favre,¹ D. Fedele,³ S. Feng,^{17,18,19} F. Fontani ³, L. Francis,^{20,21} T. Hama,^{22,23} T. Hanawa,²⁴ E. Herbst,²⁵ T. Hirota,¹⁸ M. Imai,²⁶ A. Isella,²⁷ I. Jiménez-Serra,²⁸ D. Johnstone,^{20,21} C. Kahane,¹ B. Lefloch,¹ L. Loinard,^{16,29} M. J. Maureira,¹⁰ S. Mercimek,^{3,30} A. Miotello,⁶ S. Mori,⁹ R. Nakatani,⁴ H. Nomura,³¹ Y. Oba,³² S. Ohashi,⁴ Y. Okoda,²⁶ J. Ospina-Zamudio ¹, Y. Oya,²⁶ J. Pineda ¹⁰, L. Podio ³, A. Rimola ³², D. Segura Cox,¹² Y. Shirley,³³ V. Taquet,³ L. Testi,⁶ C. Vastel,¹³ S. Viti,³⁴ N. Watanabe,³⁵ A. Witzel,¹ C. Xue,²⁵ Y. Zhang,⁴ B. Zhao ¹⁰ and S. Yamamoto²⁶

Affiliations are listed at the end of the paper

Accepted 2020 July 13. Received 2020 July 10; in original form 2020 June 2

ABSTRACT

The study of hot corinos in solar-like protostars has been so far mostly limited to the Class 0 phase, hampering our understanding of their origin and evolution. In addition, recent evidence suggests that planet formation starts already during Class I phase, which therefore represents a crucial step in the future planetary system chemical composition. Hence, the study of hot corinos in Class I protostars has become of paramount importance. Here, we report the discovery of a hot corino towards the prototypical Class I protostar L1551 IRS5, obtained within the ALMA (Atacama Large Millimeter/submillimeter Array) Large Program FAUST (Fifty AU STudy of the chemistry in the disc/envelope system of solar-like protostars). We detected several lines from methanol and its isotopologues (¹³CH₃OH and CH₂DOH), methyl formate, and ethanol. Lines are bright towards the north component of the IRS5 binary system, and a possible second hot corino may be associated with the south component. The methanol lines' non-LTE analysis constrains the gas temperature (~ 100 K), density ($\geq 1.5 \times 10^8$ cm⁻³), and emitting size (~ 10 au in radius). All CH₃OH and ¹³CH₃OH lines are optically thick, preventing a reliable measure of the deuteration. The methyl formate and ethanol relative abundances are compatible with those measured in Class 0 hot corinos. Thus, based on this work, little chemical evolution from Class 0 to I hot corinos occurs.

Key words: astrochemistry – stars: formation – ISM: molecules.

1 INTRODUCTION

Solar-like planetary systems are the result of a complex process that starts from a cold molecular cloud and evolves through various phases (e.g. Caselli & Ceccarelli 2012). Among them, the Class I protostellar stage, whose typical duration is $\leq 10^5$ yr, represents a crucial link between the youngest Class 0 and the Class II/III protostars (e.g. Crimier et al. 2010), the latter being characterized by developed protoplanetary discs. A recent ALMA breakthrough was the detection of gaps and rings in discs around protostars with ages ≤ 1 Myr (Sheehan & Eisner 2017; Fedele et al. 2018), strongly suggesting that the planet formation process starts already in Class I

protostellar discs. Since the process itself and the chemical content of the future planets, asteroids, and comets depend on the chemical composition of the disc/envelope, understanding it at the planet formation scales has become crucial.

However, despite its far-reaching importance, the chemical content of Class I protostars is, at the moment, poorly known. Class 0 protostars have infalling–rotating envelopes and circumstellar discs whose chemical composition largely, but not exclusively, depends on the distance from the central accreting object and the composition of the grain mantles (e.g. Caselli & Ceccarelli 2012; Sakai & Yamamoto 2013). Particularly relevant to this letter, Class 0 protostars possess hot corinos (Ceccarelli 2004), which are defined as warm (≥ 100 K), dense ($\geq 10^7$ cm⁻³), and compact (≤ 100 au) regions enriched in interstellar complex organic molecules (hereafter iCOMs; Ceccarelli et al. 2017). The chemical composition in these regions is believed to be the result of the sublimation of the grain mantles where the dust reaches about 100 K, regardless of the detailed geometry of the

* E-mail: eleonora.bianchi@univ-grenoble-alpes.fr (EB); cecilia.ceccarelli@univ-grenoble-alpes.fr (CC); codella@arcetri.astro.it (CC)

region, whether a spherical infalling envelope or a circumstellar disc. While about a dozen Class 0 hot corinos are imaged so far, only two Class I hot corinos are (De Simone et al. 2017; Bergner et al. 2019a; Belloche et al. 2020). More generally, few studies have focused on Class I protostars, often targeting the envelope or specific molecules (Jørgensen, Schöier & van Dishoeck 2004; Codella et al. 2016, 2018; Bianchi et al. 2017, 2019b, a; Bergner et al. 2018, 2019a, b; Artur de la Villarmois et al. 2019a; Artur de la Villarmois, Kristensen & Jørgensen 2019b; Oya et al. 2019). The scarcity of available observations makes it difficult to assess whether or not the chemical composition of Class 0 and I protostars differs. Observations of the chemical content of Class I protostars at the planet formation scale have now become urgent to understand the chemical evolution during the formation of planetary systems around solar-like stars.

In this context, the ALMA (Atacama Large Millimeter/submillimeter Array) Large Program FAUST (Fifty AU Study of the chemistry in the disc/envelope system of solar-like protostars; <http://faust-almalab.riken.jp>) is designed to survey the chemical composition of a sample of 13 Class 0/I protostars at the planet formation scale, probing regions from about 1000 to 50 au (all have a distance ≤ 250 pc). The selected sources represent the protostellar chemical diversity observed at large (≥ 1000 au) scales. All the targets are observed in three frequency set-ups chosen to study both continuum and line emission from specific molecules: 85.0–89.0, 97.0–101.0, 214.0–219.0, 229.0–234.0, 242.5–247.5, and 257.5–262.5 GHz. The FAUST survey provides a uniform sample in terms of frequency setting, angular resolution, and sensitivity. We report the first results, obtained towards the prototypical Class I protostar L1551 IRS5. This study focuses on iCOM lines and aims at discovering and studying its hot corino(s).

2 THE L1551 IRS5 SOURCE

L1551 IRS5 is located in Taurus (Strom, Strom & Vrba 1976) at a distance of 141 ± 7 pc (Zucker et al. 2019), has a $L_{\text{bol}} = 30\text{--}40 L_{\odot}$ (Liseau, Fridlund & Larsson 2005), is a FU Ori-like object (Connelley & Reipurth 2018), and is considered a prototypical Class I source (Adams, Lada & Shu 1987; Looney, Mundy & Welch 1997). It is surrounded by a large (~ 0.1 pc) rotating/infalling envelope with $A_{\text{v}} > 100$ mag (e.g. Fridlund et al. 2005; Moriarty-Schieven et al. 2006; White et al. 2006) studied via lines from several species such as CH_3OH , HCN, CS, and HCO^+ (e.g. Fridlund et al. 2002; White et al. 2006). L1551 IRS5 is associated with a molecular outflow and the HH154 jet, extensively studied in the X-ray, optical, near-IR, and radio emission (e.g. Snell, Loren & Plambeck 1980; Fridlund et al. 2005; Schneider, Günther & Schmitt 2011, and references therein). Zooming into the inner 100 au, L1551 IRS5 is a binary system, revealed for the first time by VLA cm observations (Bieging & Cohen 1985) that show two parallel jets (Rodríguez et al. 2003b). The binarity was confirmed by BIMA millimetre observations (Looney et al. 1997) that identified a northern source N ($\sim 0.8 M_{\odot}$) and a southern source S ($\sim 0.3 M_{\odot}$) (Liseau et al. 2005). The two protostars are surrounded by a circumbinary disc, whose radius and mass are ~ 140 au and $0.02\text{--}0.03 M_{\odot}$, respectively (Looney et al. 1997; Cruz-Sáenz de Miera et al. 2019). ALMA observations also suggest the presence of two dusty discs ($M_{\text{disc}} > 0.006 M_{\odot}$) towards N and S, with radii between 8 and 14 au. The protostellar discs' inclination is expected to be $\sim 35\text{--}45^{\circ}$ for N and $\sim 24\text{--}44^{\circ}$ for S (Lim et al. 2016; Cruz-Sáenz de Miera et al. 2019). Proper motion measurements show an orbital rotation of N and S with a period of ~ 260 yr and an eccentricity orbit tilted by up to 25° from the circumbinary disc (Rodríguez et al. 2003b; Lim et al. 2016).

3 OBSERVATIONS

L1551 IRS5 was observed with ALMA (FAUST Large Program 2018.1.01205.L). The data here exploited were acquired on 2018 October 25 using the C43-5 antenna configuration, with baselines between 15 m and 1.4 km. The analysed spectral window (232.8–234.7 GHz) was observed using spectral channels of 488 kHz (0.63 km s^{-1}). The observations were centred at $\alpha_{\text{J2000}} = 04^{\text{h}} 31^{\text{m}} 34^{\text{s}}.14$, $\delta_{\text{J2000}} = +18^{\circ} 08' 05''.10$. The quasar J0423–0120 was used as bandpass and flux calibrator, and J0510+1800 as phase calibrator. The data were calibrated using the ALMA calibration pipeline within CASA (McMullin et al. 2007) and we included an additional calibration routine to correct for the T_{sys} and spectral data normalization.¹ The data were self-calibrated using carefully determined line-free continuum channels, including corrections for the continuum spectral index, and the continuum model was then subtracted from the visibilities prior to imaging the line data. The resulting continuum-subtracted line cube, made using a Briggs robust parameter of 0.4, has a synthesized beam of $0.37 \text{ arcsec} \times 0.31 \text{ arcsec}$ (PA = 39°), and an rms noise of 1 mJy beam^{-1} in a 0.6 km s^{-1} channel, as expected. We estimate the absolute flux calibration uncertainty of 10 per cent and an additional error of 10 per cent for the spectra baseline determination. Spectral line imaging was performed with the CASA package, while the data analysis was performed using the IRAM-GILDAS package.

4 RESULTS

Fig. 1 shows the map towards L1551 IRS5 of the dust emission at 1.3 mm and the positions of N and S at different dates since 1983. The two objects are not clearly resolved. The deconvolved source size, derived from a 2D Gaussian fit of the emission, is around 0.4 arcsec , similar to the beam size. In addition, it is evident that N is brighter, in agreement with previous observations (Cruz-Sáenz de Miera et al. 2019). The continuum map also shows extended emission ($\sim 1 \text{ arcsec}$ in radius) associated with the circumbinary disc.

Table 1 lists the detected lines from the following iCOMs: methanol and its most abundant isotopologues (CH_3OH , $^{13}\text{CH}_3\text{OH}$, and CH_2DOH), methyl formate (HCOOCH_3), and ethanol ($\text{CH}_3\text{CH}_2\text{OH}$). In Fig. 1, we show the integrated intensity (moment 0) maps for one representative line of each molecule. For all lines, the emission peak coincides, within the synthesized beam, with the continuum position peak of source N, although fainter emission is also detected towards the southern component. The figure also shows the spectra of the $\text{CH}_3\text{OH}_{5_{4,2}\text{--}6_{3,3}}$ E line, extracted in one pixel from different positions across the region in a direction perpendicular to the jet direction. Note that the spectra of the other iCOM lines have the same behaviour.

4.1 IRS5 N

The methanol emission towards N, marked as P3 in Fig. 1, has a double-peaked profile with a central dip at $+7.5 \text{ km s}^{-1}$. The red- and blueshifted peaks seem associated with gas to the north (positions P1 and P2) and south (P4 and P5) of N, respectively. This velocity pattern, perpendicularly to the jet axis, could be due to either a rotating inner envelope or a disc. Unfortunately, since the emission is not resolved, it is impossible to discriminate between the two possibilities. The spectra of all detected iCOM lines towards

¹[https://help.almascience.org/index.php?/Knowledgebase/Article/View/419;Moellenbrock et al. \(in preparation\).](https://help.almascience.org/index.php?/Knowledgebase/Article/View/419;Moellenbrock%20et%20al.%20(in%20preparation).)

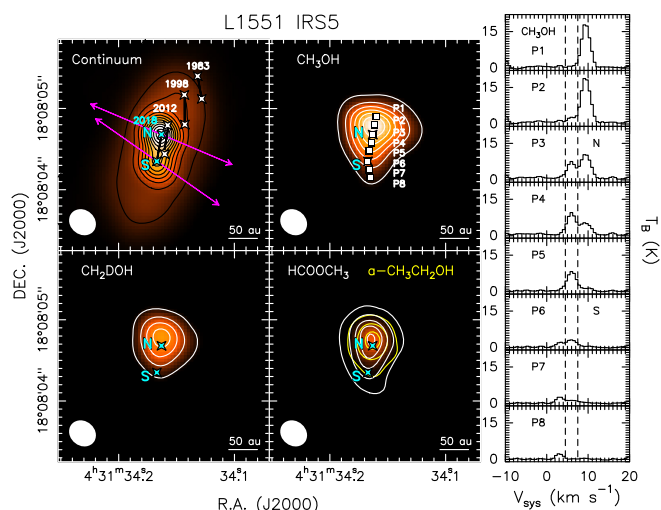


Figure 1. Dust and line emission towards L1551 IRS5. Upper left: 1.3 mm dust continuum emission in colour scale and black contours. First contours and steps are 10σ ($1.8 \text{ mJy beam}^{-1}$) and 100σ , respectively. The white stars indicate the positions of N and S measured in 1983, 1998, and 2012 (Rodríguez et al. 2003a; Lim et al. 2016), while the cyan stars refer to 2018 (this work). The magenta arrows indicate the jet directions (Rodríguez et al. 2003b). Upper right: Colour scale and white contours show the moment 0 map of the $\text{CH}_3\text{OH } 5_{4,2}-6_{3,3} \text{ E}$ line, integrated over $+2$ to $+15 \text{ km s}^{-1}$. First contours and steps are 8σ ($40 \text{ mJy beam}^{-1} \text{ km}^{-1}$) and 15σ , respectively. The white squares, labelled from P1 to P8, are the different positions where the spectra displayed on the right-hand panels are extracted. The positions P3 and P6 correspond to N and S, respectively. Lower left: Same as for the upper right panel, for the $\text{CH}_2\text{DOH } 8_{2,6}-8_{1,7} \text{ e0}$ line, integrated over $+2$ to $+15 \text{ km s}^{-1}$. First contours and steps are 8σ ($42 \text{ mJy beam}^{-1} \text{ km}^{-1}$) and 15σ , respectively. Lower right: Colour scale and yellow contours show the moment 0 map of the $a\text{-CH}_3\text{CH}_2\text{OH } 10_{5,5}-10_{4,6}$ line integrated between $+2$ and $+15 \text{ km s}^{-1}$. First contours and steps are 5σ ($42 \text{ mJy beam}^{-1} \text{ km}^{-1}$) and 10σ , respectively. White contours show the moment 0 map of the $\text{HCOOCH}_3 18_{4,14}-17_{4,13} \text{ A}$ line integrated between $+2$ and $+12 \text{ km s}^{-1}$. First contours and steps are 5σ ($28.5 \text{ mJy beam}^{-1} \text{ km}^{-1}$) and 10σ , respectively. Right-hand panel: $\text{CH}_3\text{OH } 5_{4,2}-6_{3,3}$ spectra extracted at the P1–P8 map positions. The vertical dashed lines mark the systemic velocity inferred towards N ($+7.5 \text{ km s}^{-1}$) and S ($+4.5 \text{ km s}^{-1}$), respectively.

position P3, corresponding to the N continuum peak, are shown in Fig. 2, while their spectral parameters are reported in Table 1.

4.2 IRS5 S

Similarly to N, the lines are double-peaked towards S, with a central dip at $+4.5 \text{ km s}^{-1}$, namely $\sim 3 \text{ km s}^{-1}$ redshifted with respect to N. Going south (positions P7 and P8), the red peak disappears and only the blue one remains, suggesting again emission from a rotating inner envelope or a disc, assuming that the red peak is mainly associated with S.

5 COLUMN DENSITIES AND PHYSICAL PARAMETERS

We derived the density and temperature of the gas emitting the methanol lines towards P3 (Table 1), along with the molecular abundances of the detected iCOMs. To this end, we carried out a non-LTE analysis of the CH_3OH lines via the large velocity gradient (LVG) code by Ceccarelli et al. (2003). We used the collisional coefficients of $\text{CH}_3\text{OH-A}$ and $\text{CH}_3\text{OH-E}$ with *para*- H_2 computed

Table 1. Properties of the lines detected towards L1551 IRS5.

Transition	ν^a (GHz)	E_{up}^a (K)	$S\mu^{2a}$ (D^2)	I_{int}^b (K km s^{-1})
$\text{CH}_3\text{OH } 10_{3,7}-11_{2,9} \text{ E}$	232.9458	190	12	61
$\text{CH}_3\text{OH } 18_{3,15}-17_{4,14} \text{ A}$	233.7957	447	22	54
$\text{CH}_3\text{OH } 4_{2,3}-5_{1,4} \text{ A}$	234.6834	61	4	76
$\text{CH}_3\text{OH } 5_{4,2}-6_{3,3} \text{ E}$	234.6985	123	2	49
$^{13}\text{CH}_3\text{OH } 5_{1,5}-4_{1,4} \text{ A}$	234.0116	48	4	54
$\text{CH}_2\text{DOH } 3_{3,1} \text{ e0}-4_{2,2} \text{ e0}$	232.9019	49	0.2	10
$\text{CH}_2\text{DOH } 3_{3,0} \text{ e0}-4_{2,3} \text{ e0}$	232.9290	49	0.2	34
$\text{CH}_2\text{DOH } 5_{3,2} \text{ o1}-4_{2,2} \text{ e0}$	233.0831	68	0.2	45
$\text{CH}_2\text{DOH } 5_{3,3} \text{ e0}-4_{2,3} \text{ o1}$	233.1339	68	0.2	30
$\text{CH}_2\text{DOH } 14_{2,12} \text{ o1}-14_{1,13} \text{ o1}$	233.1418	261	6	33
$\text{CH}_2\text{DOH } 9_{2,8} \text{ e1}-9_{1,9} \text{ e1}$	233.4611	123	1.5	34
$\text{CH}_2\text{DOH } 8_{2,6} \text{ e0}-8_{1,7} \text{ e0}$	234.4710	94	10	59
$\text{HCOOCH}_3 19_{4,16}-18_{4,15} \text{ A}$	233.2268	123	48	37
$\text{HCOOCH}_3 19_{14,6}-18_{14,5} \text{ E}$	233.4144	242	23	17
$\text{HCOOCH}_3 19_{12,8}-18_{12,7} \text{ E}$	233.6710	208	30	17
$\text{HCOOCH}_3 18_{4,14}-17_{4,13} \text{ E}$	233.7540	114	46	47
$\text{HCOOCH}_3 18_{4,14}-17_{4,13} \text{ A}$	233.7775	114	46	36
$\text{HCOOCH}_3 19_{11,8}-18_{11,7} \text{ E}$	233.8452	192	34	31
$\text{HCOOCH}_3 19_{11,9}-18_{11,8} \text{ E}$	233.8672	192	34	22
$\text{HCOOCH}_3 19_{10,10}-18_{10,9} \text{ E}$	234.1346	178	37	30
$\text{CH}_3\text{CH}_2\text{OH } 14_{5,9}-14_{4,10}$	232.9285	120	14	36
$\text{CH}_3\text{CH}_2\text{OH } 13_{5,8}-13_{4,9}$	233.5710	108	13	18
$\text{CH}_3\text{CH}_2\text{OH } 13_{5,9}-13_{4,10}$	233.9511	108	13	25
$\text{CH}_3\text{CH}_2\text{OH } 12_{5,8}-12_{4,9}$	234.2552	97	12	24
$\text{CH}_3\text{CH}_2\text{OH } 10_{5,5}-10_{4,6}$	234.6663	78	9	28
$\text{CH}_3\text{CH}_2\text{OH } 10_{5,6}-10_{4,7}$	234.7146	78	9	18

Note. ^aSpectroscopic parameters of CH_3OH and $^{13}\text{CH}_3\text{OH}$ are from Xu & Lovas (1997) and Xu et al. (2008), retrieved from the CDMS data base (Müller et al. 2005). Those of CH_2DOH , HCOOCH_3 , and *anti*- $\text{CH}_3\text{CH}_2\text{OH}$ are from Pearson, Brauer & Drouin (2008), Pearson, Yu & Drouin (2012), and Ilyushin, Kryvda & Alekseev (2009), retrieved from the JPL data base (Pickett et al. 1998). ^bIntegrated intensities (I_{int}) derived at the position P3 (Fig. 1). The associated errors are less than 1 K km s^{-1} .

between 10 and 200 K for the first 256 levels of each species (Rabli & Flower 2010), provided by the BASECOL data base (Dubernet et al. 2013). We assumed a spherical geometry (de Jong, Boland & Dalgarno 1980), a $\text{CH}_3\text{OH-A/CH}_3\text{OH-E}$ ratio equal to 1, a $^{12}\text{C}/^{13}\text{C}$ ratio equal to 60 (Milam et al. 2005), a line full width at half-maximum (FWHM) equal to 3.5 km s^{-1} as measured, and that the levels are populated by collisions and not by the absorption of the dust background photons whose contribution is very likely negligible due to the low values of the CH_3OH Einstein coefficients. We ran a large grid of models ($\geq 10^4$) covering a $\text{CH}_3\text{OH-A}$ ($N_{\text{CH}_3\text{OH-A}}$) and $\text{CH}_3\text{OH-E}$ column density from 3×10^{16} to $4 \times 10^{19} \text{ cm}^{-2}$, an H_2 number density (n_{H_2}) from 3×10^6 to $2 \times 10^8 \text{ cm}^{-3}$, and a gas temperature (T_{kin}) from 80 to 180 K. We found the solution with the lowest χ^2 by simultaneously fitting the $\text{CH}_3\text{OH-A}$, $\text{CH}_3\text{OH-E}$, and $^{13}\text{CH}_3\text{OH-A}$ lines, leaving the $N_{\text{CH}_3\text{OH-A}}$, n_{H_2} , T_{kin} , and the emitting size (the emission is unresolved) as free parameters. Since the collisional coefficients are available for only the three lines with the upper level energy less than 200 K, only those were used. The best fit is obtained with $N_{\text{CH}_3\text{OH-A}} = 1 \times 10^{19} \text{ cm}^{-2}$ and a size of 0.15 arcsec (21 au). Solutions with $N_{\text{CH}_3\text{OH-A}} \geq 0.5 \times 10^{19} \text{ cm}^{-2}$ are within the 1σ confidence level. All the observed CH_3OH lines are optically thick ($\tau > 50$), as well as the $^{13}\text{CH}_3\text{OH-A}$ ($\tau \sim 2$) one, which makes the size well constrained. The temperature is $100 \pm 10 \text{ K}$ and the density is $\geq 1.5 \times 10^8 \text{ cm}^{-3}$ at 1σ confidence level. The

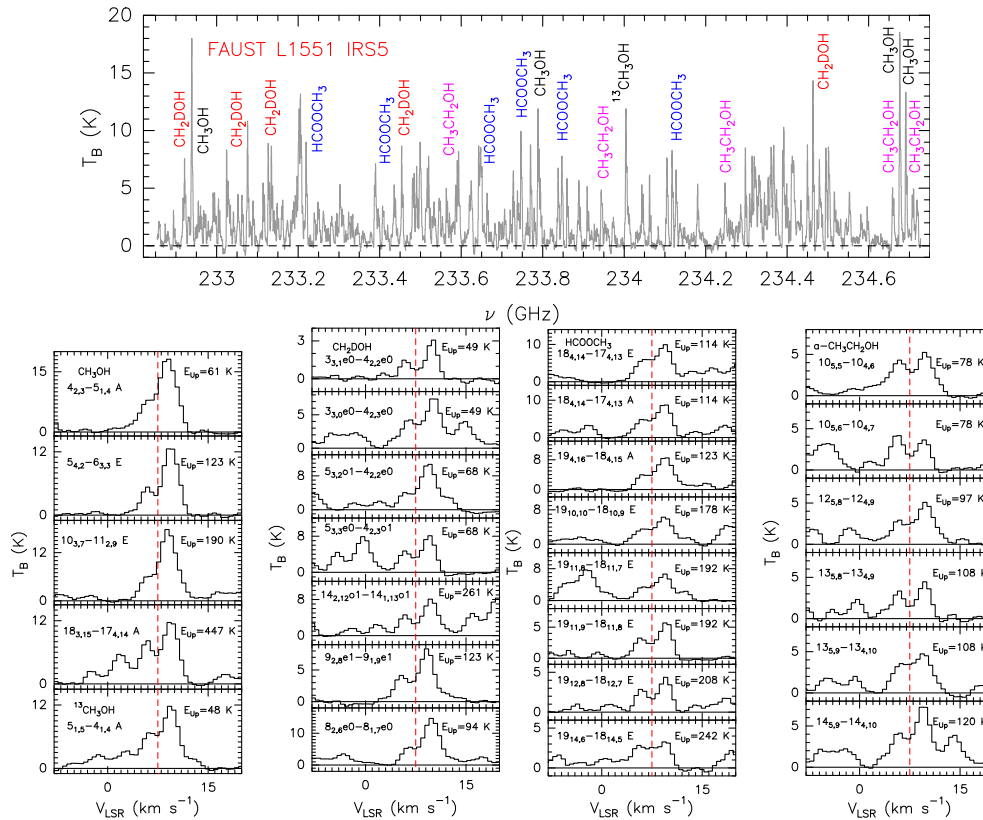


Figure 2. Observed line spectra (in T_B scale) towards IRS5 N (P3 position of Fig. 1). Upper panel: Entire spectrum between 232.8 and 234.7 GHz. Lower panels: Spectra of CH_3OH , $^{13}\text{CH}_3\text{OH}$, CH_2DOH , HCOOCH_3 , and *anti*- $\text{CH}_3\text{CH}_2\text{OH}$: transitions and upper level energies are reported in the upper left and right corners of each panel, respectively. The vertical dashed line marks the ambient LSR velocity ($+7.5 \text{ km s}^{-1}$).

results do not change if we assume a line FWHM of 3.0 or 4.0 km s^{-1} and they as the line optical depths are weakly model dependent because of the $^{13}\text{CH}_3\text{OH}$ line detection.

Collisional rates are not available for the other molecules, so we used the rotational diagram analysis to estimate their column densities, assuming a source size of 0.15 arcsec as derived from the methanol analysis. In the case of CH_2DOH , we derive a rotational temperature of $88 \pm 9 \text{ K}$ and a column density of $(64 \pm 11) \times 10^{16} \text{ cm}^{-2}$. However, as the non-LTE methanol line analysis shows that even the $^{13}\text{CH}_3\text{OH}$ line is optically thick, we expect the same for the CH_2DOH lines, so that the derived column density is a lower limit. For HCOOCH_3 and $\text{CH}_3\text{CH}_2\text{OH}$, the E_{up} range covered by the detected lines is not large enough, so we assumed a rotational temperature of 100 K, based on the methanol LVG analysis, to derive the respective column densities. They are $(33 \pm 2) \times 10^{16}$ and $(149 \pm 13) \times 10^{15} \text{ cm}^{-2}$ for methyl formate and ethanol, respectively. With these column densities, the predicted opacity is around 0.3–0.5 for the methyl formate lines and ~ 0.2 for the ethanol lines. Therefore, both column densities (Table 2) are not affected by the line opacity.

6 DISCUSSION AND CONCLUSIONS

6.1 The hot corinos of L1551 IRS5

The derived gas temperature and the detection of iCOMs make L1551 IRS5 N a hot corino. The present data also suggest the presence of a second hot corino in S, to be confirmed by higher spatial resolution observations. This increases, and perhaps doubles, the number of known Class I hot corinos as, before this work, only two were imaged,

Table 2. List of detected iCOMs towards L1551 IRS5 N.

Species	N_{lines}^a	E_{ul} (K)	T_{rot}^b (K)	N_{tot}^b (cm^{-2})
Non-LTE analysis				
CH_3OH	3	61–190	100(10)	$\geq 1 \times 10^{19c}$
$^{13}\text{CH}_3\text{OH}$	1	48		
Rotational diagram analysis				
CH_2DOH	7	49–261	88(9)	$\geq 5 \times 10^{17}$
HCOOCH_3	8	114–242	100 ^d	$33(2) \times 10^{16d}$
$\text{CH}_3\text{CH}_2\text{OH}$	6	78–120	100 ^d	149(13) $\times 10^{15d}$

Note. ^aNumber of lines used in the analysis. ^bParameters derived adopting a source size of 0.15 arcsec, as derived by the non-LTE analysis of the methanol lines. Upper limits and error bars (in parenthesis) are at 1σ confidence level. ^cTotal methanol column density. ^dTo derive the column density, we assumed T_{rot} equal to 100 K, as derived by the methanol non-LTE analysis.

SVS13-A (De Simone et al. 2017; Belloche et al. 2020) and Ser-emb 17 (Bergner et al. 2019a). Besides, our observations are the first to provide the chemical richness of Class I protostars on a Solar system scale. The derived emitting size for N of 0.15 arcsec, equivalent to about 20 au, is consistent with the heating from the central $40 L_{\odot}$ source, and does not necessarily require an outburst activity. However, note that the 0.15 arcsec sizes are derived assuming a filling factor from a circular Gaussian source emission. If the emission is more elongated in one direction, as would be the case in a rotating envelope and/or disc, this could explain the slightly more extended emission of Fig. 1.

One result of this work is that the methanol lines towards L1551 IRS5 N are very optically thick. This implies that we can only establish a lower limit to the true methanol column density. This large methanol line opacity very likely is not a unique property of L1551 IRS5 and it is even more dramatic in Class 0 protostars, with their larger material column densities with respect to Class I sources. This was already clear from the observations of IRAS 16293–2422, where $\text{CH}_3^{18}\text{OH}$ was used to derive the methanol column density (Jørgensen et al. 2016). Even more dramatically, recent VLA observations showed extremely optically thick methanol lines towards NGC 1333 IRAS 4A1 and IRAS 4A2 (De Simone et al. 2020). Here, we show that even in Class I hot corinos the estimation of the column density of methanol assuming that the ^{13}C isotopologue lines are optically thin can be inaccurate. This fact could explain the contradictory results found by Bianchi et al. (2019b) when comparing the iCOM abundances normalized to methanol in different Class 0 and I protostars. A reliable measure requires the ^{18}O methanol isotopologue detection.

Finally, given the high line optical depths, we cannot estimate the methanol deuteration, because both the derived methanol and deuterated methanol column densities are lower limits, $\geq 1 \times 10^{19}$ and $\geq 5 \times 10^{17} \text{ cm}^{-2}$, respectively. Taking these at face value, methanol deuteration would be of 5 per cent. Again, to obtain a reliable measure requires the detection of $^{13}\text{CH}_2\text{DOH}$.

6.2 Methyl formate and ethanol in Class 0 and I sources

The methyl formate and ethanol abundances relative to methanol are ≤ 0.03 and ≤ 0.015 , respectively (Table 2). The methyl formate normalized abundance is compatible with that measured, at comparable spatial scales, towards the Class 0 hot corinos IRAS 16293–2122B (0.03; Jørgensen et al. 2018), HH212 (0.03; Lee et al. 2019), and IRAS 4A and IRAS 2A (0.005 and 0.016; Taquet et al. 2015; López-Sepulcre et al. 2017). The ethanol normalized abundance in L1551 IRS5 N is also similar to the normalized abundances measured in the Class 0 hot corinos mentioned above, namely 0.006–0.02. Finally, both methyl formate and ethanol normalized abundances are similar to those measured in the Class I hot corino of SVS13-A, 0.016 and 0.014, respectively (Bianchi et al. 2019b). A more reliable comparison can be obtained by considering the abundance ratio between methyl formate and ethanol, which are both optically thin. In L1551 IRS5 N, this value is ~ 2 , a factor of 2 larger than that measured in the Class 0 IRAS 16293–2122B (Jørgensen et al. 2018) and Class I SVS13-A (Bianchi et al. 2019b). Considering all the uncertainties, the Class I L1551 IRS5, similarly to SVS13-A, does not look dramatically different from Class 0 hot corinos with respect to the iCOM relative abundances.

ACKNOWLEDGEMENTS

This project has received funding from (1) the European Research Council (ERC) under the European Union’s Horizon 2020 research and innovation program, for the Project ‘The Dawn of Organic Chemistry’ (DOC), grant agreement no. 741002; (2) the PRIN-INAF 2016 ‘The Cradle of Life – GENESIS-SKA (General Conditions in Early Planetary Systems for the Rise of Life with SKA)’; (3) a Grant-in-Aid from Japan Society for the Promotion of Science (KAKENHI: numbers 18H05222, 19H05069, and 19K14753); (4) the Spanish FEDER under project no. ESP2017-86582-C4-1-R; (5) DGAPA, UNAM grants IN112417 and IN112820, and CONACYT, Mexico; (6) ANR of France under contract no. ANR-16-CE31-0013; (7) the French National Research Agency in the framework of the

Investissements d’Avenir program (ANR-15-IDEX-02), through the funding of the ‘Origin of Life’ project of the Univ. Grenoble-Alpes; and (8) the European Union’s Horizon 2020 research and innovation programs under projects ‘Astro-Chemistry Origins’ (ACO), grant no. 811312. This paper makes use of the following ALMA data: ADS/JAO.ALMA#2018.1.01205.L. ALMA is a partnership of ESO (representing its member states), NSF (USA), and NINS (Japan), together with NRC (Canada), MOST and ASIAA (Taiwan), and KASI (Republic of Korea), in cooperation with the Republic of Chile. The Joint ALMA Observatory is operated by ESO, AUI/NRAO, and NAOJ. The National Radio Astronomy Observatory is a facility of the National Science Foundation operated under cooperative agreement by Associated Universities, Inc. We thank the referee, Paul Ho, for his insightful suggestions.

DATA AVAILABILITY

The raw data will be available on the ALMA archive at the end of the proprietary period (ADS/JAO.ALMA#2018.1.01205.L).

REFERENCES

- Adams F. C., Lada C. J., Shu F. H., 1987, *ApJ*, 312, 788
 Artur de la Villarmois E., Jørgensen J. K., Kristensen L. E., Bergin E. A., Harsono D., Sakai N., van Dishoeck E. F., Yamamoto S., 2019a, *A&A*, 626, A71
 Artur de la Villarmois E., Kristensen L. E., Jørgensen J. K., 2019b, *A&A*, 627, A37
 Belloche A. et al., 2020, *A&A*, 635, A198
 Bergner J. B., Guzmán V. G., Öberg K. I., Loomis R. A., Pegues J., 2018, *ApJ*, 857, 69
 Bergner J. B., Martín-Doménech R., Öberg K. I., Jørgensen J. K., Artur de la Villarmois E., Brinch C., 2019a, *ACS Earth Space Chem.*, 3, 1564
 Bergner J. B., Öberg K. I., Walker S., Guzmán V. V., Rice T. S., Bergin E. A., 2019b, *ApJ*, 884, L36
 Bianchi E. et al., 2017, *MNRAS*, 467, 3011
 Bianchi E., Ceccarelli C., Codella C., Enrique-Romero J., Favre C., Lefloch B., 2019a, *ACS Earth Space Chem.*, 3, 2659
 Bianchi E. et al., 2019b, *MNRAS*, 483, 1850
 Bieging J. H., Cohen M., 1985, *ApJ*, 289, L5
 Caselli P., Ceccarelli C., 2012, *A&AR*, 20, 56
 Ceccarelli C., 2004, in Johnstone D., Adams F. C., Lin D. N. C., Neufeld D. A., Ostriker E. C., eds, *ASP Conf. Ser. Vol. 323, Star Formation in the Interstellar Medium: In Honor of David Hollenbach, Chris McKee and Frank Shu*. Astron. Soc. Pac., San Francisco, p. 195
 Ceccarelli C., Maret S., Tielens A. G. G. M., Castets A., Caux E., 2003, *A&A*, 410, 587
 Ceccarelli C. et al., 2017, *ApJ*, 850, 176
 Codella C. et al., 2016, *A&A*, 586, L3
 Codella C. et al., 2018, *A&A*, 617, A10
 Connelley M. S., Reipurth B., 2018, *ApJ*, 861, 145
 Crimier N. et al., 2010, *A&A*, 516, A102
 Cruz-Sáenz de Miera F., Kóspál Á., Ábrahám P., Liu H. B., Takami M., 2019, *ApJ*, 882, L4
 de Jong T., Boland W., Dalgarno A., 1980, *A&A*, 91, 68
 De Simone M. et al., 2017, *A&A*, 599, A121
 De Simone M. et al., 2020, *ApJ*, 896, L3
 Dubernet M.-L. et al., 2013, *A&A*, 553, A50
 Fedele D. et al., 2018, *A&A*, 610, A24
 Fridlund C. V. M., Bergman P., White G. J., Pilbratt G. L., Tauber J. A., 2002, *A&A*, 382, 573
 Fridlund C. V. M., Liseau R., Djupvik A. A., Hultgren M., White G. J., Favata F., Giardino G., 2005, *A&A*, 436, 983
 Ilyushin V., Kryvda A., Alekseev E., 2009, *J. Mol. Spectrosc.*, 255, 32
 Jørgensen J. K., Schöier F. L., van Dishoeck E. F., 2004, *A&A*, 416, 603
 Jørgensen J. K. et al., 2016, *A&A*, 595, A117

- Jørgensen J. K. et al., 2018, *A&A*, 620, A170
- Lee C.-F., Codella C., Li Z.-Y., Liu S.-Y., , 2019, *ApJ*, 876, 63
- Lim J., Yeung P. K. H., Hanawa T., Takakuwa S., Matsumoto T., Saigo K., 2016, *ApJ*, 826, 153
- Liseau R., Fridlund C. V. M., Larsson B., 2005, *ApJ*, 619, 959
- Looney L. W., Mundy L. G., Welch W. J., 1997, *ApJ*, 484, L157
- López-Sepulcre A. et al., 2017, *A&A*, 606, A121
- McMullin J. P., Waters B., Schiebel D., Young W., Golap K., 2007, in Shaw R. A., Hill F., Bell D. J., eds, *ASP Conf. Ser. Vol. 376, Astronomical Data Analysis Software and Systems XVI*. Astron. Soc. Pac., San Francisco, p. 127
- Milam S. N., Savage C., Brewster M. A., Ziurys L. M., Wyckoff S., 2005, *ApJ*, 634, 1126
- Moriarty-Schieven G. H., Johnstone D., Bally J., Jenness T., 2006, *ApJ*, 645, 357
- Müller H. S. P., Schlöder F., Stutzki J., Winnewisser G., 2005, *J. Mol. Struct.*, 742, 215
- Oya Y. et al., 2019, *ApJ*, 881, 112
- Pearson J. C., Brauer C. S., Drouin B. J., 2008, *J. Mol. Spectrosc.*, 251, 394
- Pearson J. C., Yu S., Drouin B. J., 2012, *J. Mol. Spectrosc.*, 280, 119
- Pickett H. M., Poynter R. L., Cohen E. A., Delitsky M. L., Pearson J. C., Müller H. S. P., 1998, *J. Quant. Spectrosc. Radiat. Transfer*, 60, 883
- Rabli D., Flower D. R., 2010, *MNRAS*, 406, 95
- Rodríguez L. F., Curiel S., Cantó J., Loinard L., Raga A. C., Torrelles J. M., 2003a, *ApJ*, 583, 330
- Rodríguez L. F., Porras A., Claussen M. J., Curiel S., Wilner D. J., Ho P. T. P., 2003b, *ApJ*, 586, L137
- Sakai N., Yamamoto S., 2013, *Chem. Rev.*, 113, 8981
- Schneider P. C., Günther H. M., Schmitt J. H. M. M., 2011, *A&A*, 530, A123
- Sheehan P. D., Eisner J. A., 2017, *ApJ*, 851, 45
- Snell R. L., Loren R. B., Plambeck R. L., 1980, *ApJ*, 239, L17
- Strom K. M., Strom S. E., Vrba F. J., 1976, *AJ*, 81, 320
- Taquet V., López-Sepulcre A., Ceccarelli C., Neri R., Kahane C., Charnley S. B., 2015, *ApJ*, 804, 81
- White G. J., Fridlund C. W. M., Bergman P., Beardmore A., Liseau R., Price M., Phillips R. R., 2006, *ApJ*, 651, L41
- Xu L.-H., Lovas F. J., 1997, *J. Phys. Chem. Ref. Data*, 26, 17
- Xu L.-H. et al., 2008, *J. Mol. Spectrosc.*, 251, 305
- Zucker C., Speagle J. S., Schlafly E. F., Green G. M., Finkbeiner D. P., Goodman A. A., Alves J., 2019, *ApJ*, 879, 125
- ¹IPAG, Univ. Grenoble Alpes, CNRS, F-38000 Grenoble, France
- ²National Radio Astronomy Observatory, PO Box O, Socorro, NM 87801, USA
- ³INAF, Osservatorio Astrofisico di Arcetri, Largo E. Fermi 5, I-50125 Firenze, Italy
- ⁴RIKEN Cluster for Pioneering Research, 2-1, Hirosawa, Wako-shi, Saitama 351-0198, Japan
- ⁵Institut de Radioastronomie Millimétrique, F-38406 Saint-Martin d'Hères, France
- ⁶European Southern Observatory, Karl-Schwarzschild Str 2, D-85748 Garching bei München, Germany
- ⁷Materials Science and Engineering, College of Engineering, Shibaura Institute of Technology, 3-7-5 Toyosu, Koto-ku, Tokyo 135-8548, Japan
- ⁸Graduate School of Informatics and Engineering, The University of Electro-Communications, Chofu, Tokyo 182-8585, Japan
- ⁹Department of Astronomy, The University of Tokyo, 7-3-1 Hongo, Bunkyo-ku, Tokyo 113-0033, Japan
- ¹⁰Max-Planck-Institut für extraterrestrische Physik (MPE), Gießenbachstr 1, D-85741 Garching, Germany
- ¹¹Department of Chemistry, Biology, and Biotechnology, The University of Perugia, Via Elce di Sotto 8, I-06123 Perugia, Italy
- ¹²Center for Astrochemical Studies, Max-Planck-Institut für extraterrestrische Physik (MPE), Gießenbachstr 1, D-85741 Garching, Germany
- ¹³IRAP, Université de Toulouse, CNRS, CNES, UPS, Toulouse 31400, France
- ¹⁴Astrochemistry Laboratory, Code 691, NASA Goddard Space Flight Center, 8800 Greenbelt Road, Greenbelt, MD 20771, USA
- ¹⁵CY Cergy Paris Université, Sorbonne Université, Observatoire de Paris, PSL University, CNRS, LERMA, F-95000 Cergy, France
- ¹⁶Instituto de Radioastronomía y Astrofísica, Universidad Nacional Autónoma de México, A.P. 3-72 (Xangari), Morelia 8701, Mexico
- ¹⁷CAS Key Laboratory of FAST, National Astronomical Observatory of China, Datun Road 20, Chaoyang, Beijing 100012, China
- ¹⁸National Astronomical Observatory of Japan, National Institutes of Natural Sciences, 2-21-1 Osawa, Mitaka, Tokyo 181-8588, Japan
- ¹⁹Academia Sinica Institute of Astronomy and Astrophysics, No.1, Section 4, Roosevelt Rd, Taipei 10617, Taiwan
- ²⁰Department of Physics and Astronomy, University of Victoria, 3800 Finnerty Road, Elliot Building, Victoria, BC V8P 5C2, Canada
- ²¹NRC Herzberg Astronomy and Astrophysics, 5071 West Saanich Road, Victoria, BC V9E 2E7, Canada
- ²²Komaba Institute for Science, The University of Tokyo, 3-8-1 Komaba, Meguro, Tokyo 153-8902, Japan
- ²³Department of Basic Science, The University of Tokyo, 3-8-1 Komaba, Meguro, Tokyo 153-8902, Japan
- ²⁴Center for Frontier Science, Chiba University, 1-33 Yayoi-cho, Inage-ku, Chiba 263-8522, Japan
- ²⁵Department of Chemistry, University of Virginia, McCormick Road, PO Box 400319, Charlottesville, VA 22904, USA
- ²⁶Department of Physics, The University of Tokyo, 7-3-1, Hongo, Bunkyo-ku, Tokyo 113-0033, Japan
- ²⁷Department of Physics and Astronomy, Rice University, 6100 Main Street, MS-108, Houston, TX 77005, USA
- ²⁸Centro de Astrobiología (CSIC-INTA), Ctra. de Torrejón a Ajalvir, km 4, E-28850 Torrejón de Ardoz, Spain
- ²⁹Instituto de Astronomía, Universidad Nacional Autónoma de México, Ciudad Universitaria, A.P. 70-264, Cuidad de México 04510, Mexico
- ³⁰Dipartimento di Fisica e Astronomia, Università degli Studi di Firenze, via G. Sansone 1, I-50019 Sesto Fiorentino, Italy
- ³¹Division of Science, National Astronomical Observatory of Japan, 2-21-1 Osawa, Mitaka, Tokyo 181-8588, Japan
- ³²Departament de Química, Universitat Autònoma de Barcelona, E-08193 Bellaterra, Spain
- ³³Steward Observatory, 933 N Cherry Avenue, Tucson, AZ 85721, USA
- ³⁴Department of Physics and Astronomy, University College London, Gower Street, London WC1E 6BT, UK
- ³⁵Institute of Low Temperature Science, Hokkaido University, N19W8, Kita-ku, Sapporo, Hokkaido 060-0819, Japan

This paper has been typeset from a \LaTeX file prepared by the author.